ILASS 2008
Sep. 8-10, 2008, Como Lake, Italy

Paper ID ILASS08-1-8

ANALYSIS OF MULTIPHASE FLOW DURING THE PROCESS OF SHEET DISINTEGRATION AT HOLLOW CONE NOZZLES USING MULTIPLE ONE-DIMENSIONAL FIBRE-SENSORS

*E. Musemic, *P. Walzel, °M. Gaspar, °F. Weichert

*Lehrstuhl Mechanische Verfahrenstechnik, Fakultät Bio- und Chemieingenieurwesen, Technische Universität Dortmund, Emil-Figge-Str. 68, 44227 Dortmund, Germany, E-Mail: Emir.Musemic@bci.tu-dortmund.de
°Lehrstuhl VII, Fakultät Informatik, Technische Universität Dortmund, Otto-Hahn-Str. 16, 44227 Dortmund, Germany, E-Mail: gaspar@ls7.cs.uni-dortmund.de

ABSTRACT
This work deals with the experimental analysis of multiphase flows during the process of sheet disintegration at Hollow Cone Nozzles. The characterization of surface waves and their propagation is based on the analysis of the sheet movement using multiple 1-dimensional fibre sensors. Each sensor is made of multi-mode PMMA fibers with an outer diameter of 250 micron. The main concept of the measuring technique exploits the Fresnel effect to detect the phase-change on the fibre tip, which is caused by the movement of the liquid sheet along 1-dimensional fibre-arrays. The wavelength, the wave growth rate, the amplitude and sheet velocity in main flow direction of the moving sheet have been analyzed with 8 and 15 mm - orifice nozzles. The Wavelet analysis of the sheet oscillation shows dominating oscillation frequencies within the range of $10 < f < 500$ Hz at each flow condition and nozzle geometry within the range of $0.03 < \Delta p < 0.16$ MPa differential pressure. There is also a significant decrease in the sheet velocity along its running length, probably caused by an increased "roughness" of the oscillating sheet at low liquid viscosities intensifying the interaction with the environmental gas. Increased viscosity, i.e. decreasing oscillation frequencies lead to significant extension of the break-up length of the sheet, until the disintegration finally enters into the region of rim contraction.

1 INTRODUCTION

Hollow cone nozzles (HCN) are found in various engineering applications, due to their good atomization performance and geometrical simplicity. They are used in a wide range of applications, such as spray-drying in the chemical industry, agricultural spraying, oil-fired chambers and gas turbines, scrubbing of dust and gas, etc. The nozzle designs vary from application to application within wide ranges of atomizer sizes and component geometries, although the basic concept is identical. The liquid usually enters the spin chamber of the nozzle tangentially producing a cyclone-like internal flow, also including an air core. Due to the spin flow, the liquid detaches from the orifice as a thin hyperbolical sheet. As the film propagates, it becomes wavy due to the aerodynamic stimulation in the ambient gas, linked to growth of amplitudes along streamlines. When the liquid sheet becomes unstable, it beaks up into fragments, which later on resolve to single droplets.

The estimation of drop size distributions caused by sheet fragmentation can be performed i. a. based on experimental data, such as oscillation frequencies and wavelengths leading to break up. The performance characteristics of the atomizer are directly influenced by the atomizer geometry, liquid properties and operational conditions. Hence, the prediction of droplet distributions needs a physical understanding of both, the internal flow inside the nozzle and the mechanisms of spray formation outside the nozzle. Despite extended research on the drop formation process, there is no universally valid description of the sheet break-up mechanism. In general, the wave growth process of sinusoidal waves has been examined with a linear stability theory by several authors (Squire [1], Dombrowski and Johns [2], Senecal [3]). Newer theoretical approaches consider three dimensional effects, such as the presence of lateral waves, which are found to have a considerable influence on the sheet disintegration process (Mehring and Sirignano [4], Tharakan und Ramamurthi [5]). An experimental reliable evidence of conformity to the different theoretical approaches could not yet be presented so far. Hence, satisfactory calculation methods for the drop size are not yet available, because of the highly demanding task for the measuring technique. Detailed experimental data of the flow could help to verify and improve the existing theoretical approaches.

This work deals with the experimental analysis of multiphase flows during the process of sheet disintegration at Hollow Cone Nozzles. The characterization of surface waves and their propagation is based on the analysis of the sheet movement using multiple 1-dimensional fibre sensors. The analysis covers the velocity, the dominating frequencies and growth rates of the moving sheet along the main streamlines, as well as their break-up-length. The liquid pressure and viscosity were graduated, so that a total range of Re_p between 10^3 and $2.0 \cdot 10^6$ was covered. In order to examine the influence of the nozzle geometry on the sheet disintegration process, four different nozzle geometries have been analyzed.

2 EXPERIMENTAL SETUP

All experiments were performed with different water-glycerol mixtures, with varying viscosities between $1 < \eta_L < 50$ mPas. The surface tension of all glycerol-water mixtures was nearly constant, i.e., $69 < \sigma < 71$ mN/m, therefore the differences in surface tension are assumed to have a negligible effect on the sheet behavior. The liquid pressure was graduated in steps between $0.03 < \Delta p < 0.16$ MPa.

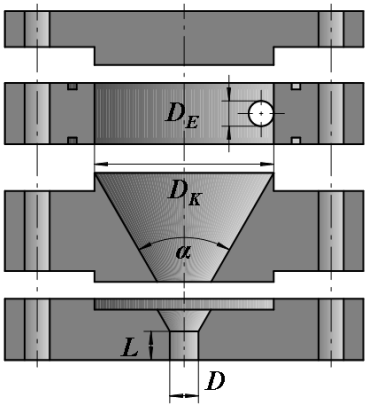

D = 8 mm; 15 mm

L/D = 0; 1

D_E = 2 x 7mm

D_K = 50 mm

α = 60 deg

Figure 1: Dimensions of the model pressure swirl nozzles

The experimental setup consists of the measuring unit and the atomization system, which allows the operation at different pressures and temperatures, as well as of different nozzles. The experimental fluid is collected in an open reservoir and conveyed to the nozzle with a rotary pump in a recycle loop. The different nozzle geometries are realized by fitting different nozzle parts from a kit. The number of inlet ports, dimensions of the swirl chamber and outlet geometry could be changed independently. In this paper, only the geometry of the nozzle orifice has been varied. Two different orifice diameters (8 and 15 mm) and orifice lengths were analyzed.

The measuring unit is based on the fiber technology, whereas the main concept of the measuring technique exploits the Fresnel effect on the plane fiber end to detect differences in the refractive index. In the present case, such differences are caused by the phase-change on the fibre tip, when the fiber is positioned inside a multiphase flow [6]. When light is coupled into the fiber on one side, the intensity of the reflected light on the other end of the fiber depends on the refractive index of the fiber environment. The intensity of the reflected light can be measured with a photo diode on the remote tip of the fiber, as the fiber is transmitter and receiver at the same time. If the refractive index of the fiber core material and the fiber environment are the same, almost all coupled light is emitted. With increasing difference in the refractive index, the fraction of the reflected light on the fiber tip also increases.

In this work, multiple fibers were bundled to a 1-dimensional array in the shape of a comb, allowing for detection of phase-changes along a line. In order to read sheet oscillations, the 1-dimensional array is positioned perpendicular to the flow trajectories as well as to the direction of the oscillating liquid sheet plane (Fig. 2). Each sensor is made of multi-mode PMMA fibers with an outer diameter of 250 micron. The light source is a laser diode forming a light sheet, which is focused and coupled into the fibers by using a bending coupler device [7]. This coupler consists of a metal wedge with an angle of 30 deg. All fibers are parallel oriented and bend together around the sharp edge of the wedge. A system of lenses flattens the laser beam from the diode to a light-sheet and focuses it to the sharp bend of the fibers. The coupled light is reflected at the interface between the fiber core material and the environmental fluid and is recorded by a line-scan CCD camera directly mounted at the remote tip of the fibers. The camera model is a DALSA Piranha 1 with a maximum sampling rate of 11 kHz. The length of such array is adapted to the expected amplitudes of the examined oscillating sheet, i. e. up to 35 mm. In addition, two of such fiber-arrays are arranged in parallel, but with an offset between particular fiber tips (Fig. 3(a)) of 11 mm in flow direction. This arrangement allows the measurement of sheet velocities, since the recorded oscillations show a phase difference (Fig. 3, (b)). As the frame rate of the used camera device is known, the phase difference can be converted into sheet velocities.

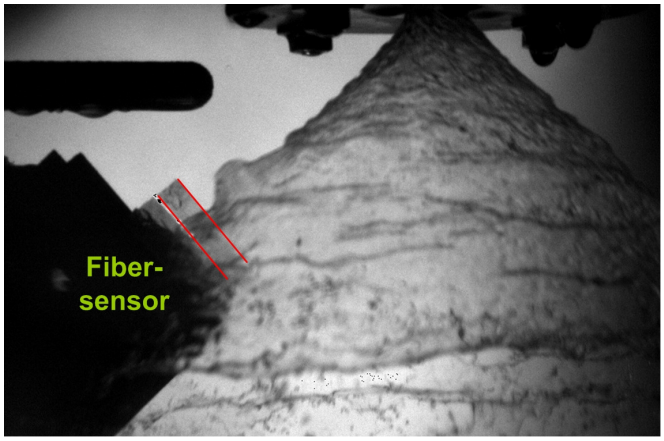

Figure 2: Invasive application of the fiber-sensor inside the oscillating liquid sheet (HCN, D=15 mm, Δp = 0.05 MPa)

With this setup the motion of the oscillating sheet impinging on the sensor is recorded with a resolution of 250 µm in space and 90 µs in time. The measuring system permits measurement of sheet velocities at every single position along the main streamline of the moving sheet, except positions very close to the nozzle due to the sensor dimensions. Since the sensor is of an invasive kind, the sensor tip is in permanent contact with the fluid and therefore a fast de-wetting of the fiber surface is desired. For this purpose, the cladding of the fiber sensor has been covered with a hydrophobic fluor-polymer, so that the improved drain off of polar fluids from the sensor tip leads to improved image quality of the recorded images.

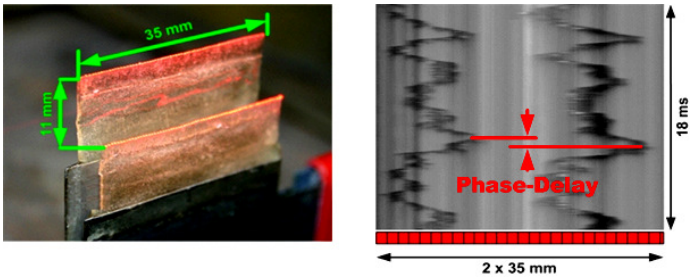

Figure 3: (a) Design of the multiple one-dimensional fibre-arrays, (b) Raw image of the oscillating liquid sheet impinging on the sensor tip recorded via line-scan CCD camera

3 SIGNAL EXTRACTION

Our aim is to represent the recorded oscillations in terms of a discrete function assigning each discrete time step a sheet displacement, which is later analyzed and evaluated. The raw data are gray level images of dimension 6000×4092 pixel as shown by an exemplary cutout in Fig. 4 (a). Each column of the image represents a time step showing the recorded fiber responses in its rows. The extraction of an analyzable signal

from the raw images is performed by the following image processing steps.

At first, the given raw image is binarized to separate the sheet contour from the background. Therefore the horizontal image gradient is computed and tresholded to identify pixel representing the position of the sheet by means of sharp gray level transitions along the time axis. The vertical image gradient is ignored, since every single fiber produces intensity gradients along the fiber array that generally can not be distinguished from sheet-position induced gradients. The resulting binarized image is filtered by a median and a morphological filter to reduce noise effects. The resulting image shows a scattered version of the signal to extract (Fig. 4, (b)).

In the past, existing systems for frequency analysis of surface waves at hollow cone nozzles have the principal disadvantage of manual interaction by the user [7]. In order to meet the demand of automatic segmentation, the second step consists of approximating the signal that is indicated by scattered unconnected image regions by means of a dual active contour approach ("snake") [8]. Thereby, the amount of manual interaction is reduced significantly to accelerate the image evaluation process. A snake is an energy minimizing curve guided by external constraint forces and influenced by image forces that direct it towards desired image features, such as lines and edges. The evolution of the active contour in the image is determined by minimizing the energy functional:

$$E_{snake}(v) = \int_0^1 E_{\text{int}}(v(s))ds + \int_0^1 E_{ext}(v(s))ds + \int_0^1 E_{user}(v(s))ds \qquad (1)$$

in which the total Energy E_{snake} of a parametric curve v(s), with s = [0,1], is separated into three components E_{ext}, E_{int} and E_{user}, specifying the state of the curve v(s). E_{int} is defined as the strain and curvature energy of the curve:

$$E_{\text{int}}(v) = \int_0^1 a\left\|\frac{\partial}{\partial s}v(s)\right\|^2 + \int_0^1 b\left\|\frac{\partial^2}{\partial s^2}v(s)\right\|^2 ds \qquad (2)$$

where a and b are constants which specify the resistance of the curve against stretching and bending. In order to guide the curve to desired image features, an external energy term E_{ext} has to be supplied. The last term of Eq. (1) may be used for imposing user-controlled constrains of the curve [8]. In the present approach, an additional force induces the two curves to move towards each other. Finally, the solution of partial differential equations associated with the active contour is computed by a finite difference scheme [9]. The dual active contour is initialised at the top (curve v_o) and bottom (curve v_u) of the image (Fig. 2, (c)). The approximation of the signal by an active contour is stopped when the movement of the curve between two time steps is below a given threshold, indicating a local minimum of the curve energy, c.f. Eq. (1). The final state of the approximation progress is shown in Fig. 4 (d). An intermediate signal is calculated from the final curves v_o and v_u to reduce artifacts. Following, all curves can be sampled and plotted as a discrete time/space-plot, which is the basis of further data evaluation.

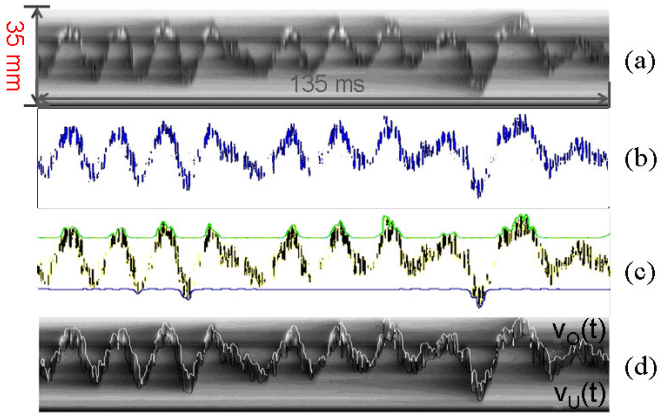

Figure 4: (a) raw image of a recorded oscillation (cutout) (b) binarized raw image indicating the sheet oscillation (c) intermediate step of contour tracking via parametric curves ("snakes") (d) raw image with the extracted sheet signal overlayed

4 DATA EVAULATION

Five pictures were recorded for every nozzle geometry, operation setting and sensor location along the moving sheet. The recorded time period of every single image is 0.54 seconds (6000 pixel). As described before, every image contains two oscillation records, which are phase-delayed due to the sensor layout (Fig. 3). Every single signal has been extracted in the same way, so that the phase-delay can be identified via cross-correlation as shown in Fig. 5.

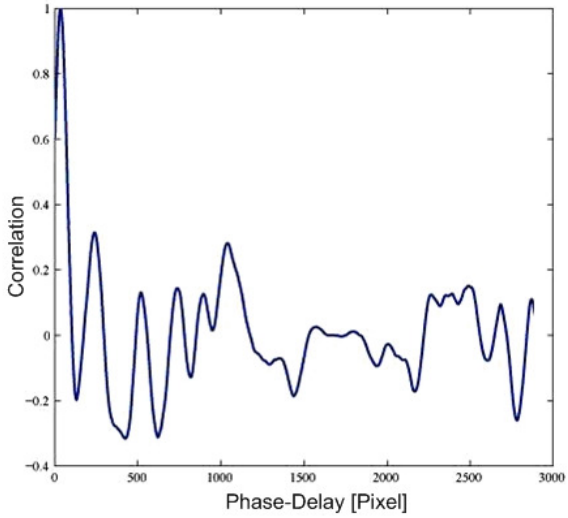

Figure 5: Phase-delay of two recorded signals identified via cross-correlation

In this case, the highest matching is found when phase-delay amounts to 25 pixels. Once the phase delay has been analyzed for every image, the velocity of the moving sheet can be identified, since the frame rate of the camera system is known (11 kHz). This means that in the present case the sheet velocity is around 3 m/s. The highest oscillation amplitude found on the liquid sheet can simply be calculated with the given geometry of the used line scan camera (4 cm = 4096 pixel). If there is some discontinuity in the recorded signal, for example when the sheet is breaking up, the active contours will stack on each other, since a collision check prevents the active contours to interpenetrate. This feature was used to

detect the position of the sheet breakup along the main flow direction. Because of a smooth transition between continuous sheet and sheet breakup, the break-up location is defined at the place, where the signal-continuity is around 50%.

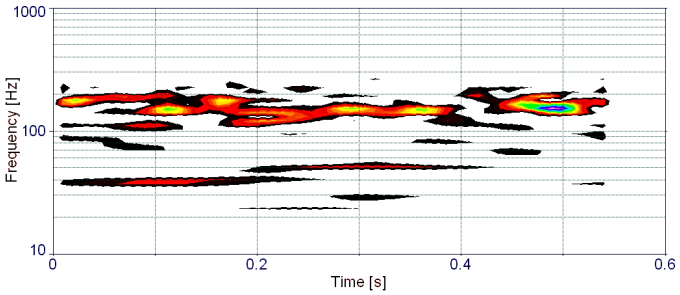

Figure 6: Example of identifying the dominating frequency bands on the oscillating sheet using Morlet-Wavelet

The oscillation frequencies found on the moving liquid sheet are of major importance when it comes to describe its disintegration or to predict the resulting droplet sizing. In the past, many authors have shown a direct link between the drop size and the dominating oscillation frequencies. Since we successfully recorded and extracted the oscillations of liquid sheets under different operating parameters, a frequency analysis of the data was made. For this purpose, we used simple Morlet-Wavelets, so that the frequencies found in the signal are plotted by their oscillation intensities along the recorded time period, as shown in Fig. 6. The advantage of the Wavelet analysis over the Fourier analysis is the resolution in time. Hence single peaks with great energy content (high amplitude) can be differentiated from continuous oscillations, which can be found within the whole time period. At example, Fig. 6 shows an oscillation signal of 0.54 s time length, which is produced by 15 mm nozzle with an L/D-ratio of 1, operating at Δp = 0.13 MPa The position of the fiber sensor was set at the end of the continuous liquid sheet, where the sheet breakup is initiating. With this setting, we found oscillation frequencies within a range of 10-500 Hz. In this case, frequencies with highest energy content are found around 150 Hz, resulting in a wavelength of 3.5 cm when the sheet velocity is considered. At least, we found the same wavelengths on simple CCD-images [10].

5 RESULTS

During the course of this study, local sheet velocities, oscillation frequencies, break-up lengths and wave spatial growths were determined experimentally. Clark and Dombrowski [11] state that while some theoretical background exists for predicting wave lengths, the unknown nature of the random turbulent motions at the interface makes it nearly impossible to specify the amplitude of disturbances initiating wave growth. They suggest values for initial disturbances between 10^{-8} m (order of molecular dimensions) and 10^{-12} m to fit theoretical sheet break-up lengths to experimental data. The spacial growth is expected to have an exponential trend, when the liquid is assumed to be inviscid. The current investigations focus on the spacial growth of these disturbances (amplitudes), to quantify the influence the liquid viscosity. Fig. 7 shows the spacial growth of the initial disturbances, as an example, for one nozzle geometry and different liquid viscosities. For low viscosities, the assumption of an exponential growth is found to be valid, even if the viscosity increases to values of around 10 mPas. This also corresponds to the viscosity of η_L = 11.3 mPas considering the higher density of the glycerol-water mixture (about 15.9 %) resulting in a higher Weber-number.

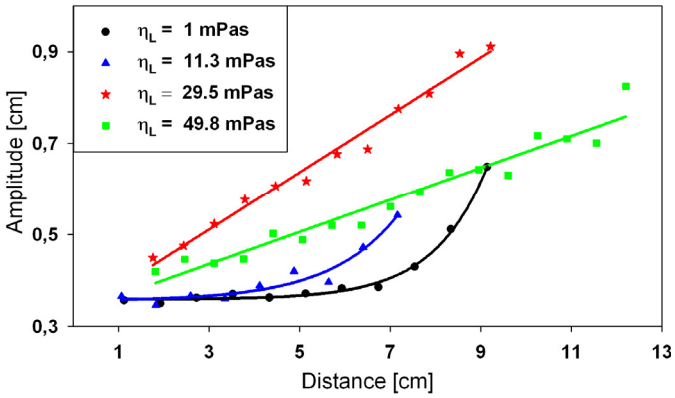

Figure 7: Amplitude height on liquid sheets depending on the distance from the orifice (D=15 mm, L/D = 1, Δp= 0.13 MPa)

If the viscosity of the atomized liquid is increased towards η_L = 29.5 mPas, there is a change over to an almost linear progression with even higher growth rates. Increasing the liquid viscosity beyond η_L = 29.5 mPas results in a slightly reduced growth rate, keeping its linear course. Similar characteristics are found when plotting the spatial growth for other nozzle geometries, although amplitude readings with the nozzles with smaller diameters (8 mm) tend to an almost linear behaviour. The same tendency is found when reducing the pressure difference. Further experiments with a larger variation of liquid viscosities will be necessary to locate the point of transition from exponential to linear course.

Similar characteristics are found when plotting the sheet break-up lengths, as shown in Fig. 8. In order to combine the different operation parameters, the Pressure-Reynolds number has been introduced, where~~at~~ the velocity of the common Reynolds-number is substituted by the Bernoulli-velocity. In addition to that, the pressure is included in the figure. The data of two different nozzle geometries are presented, with the only variation in the nozzle orifice length-diameter-ratio.

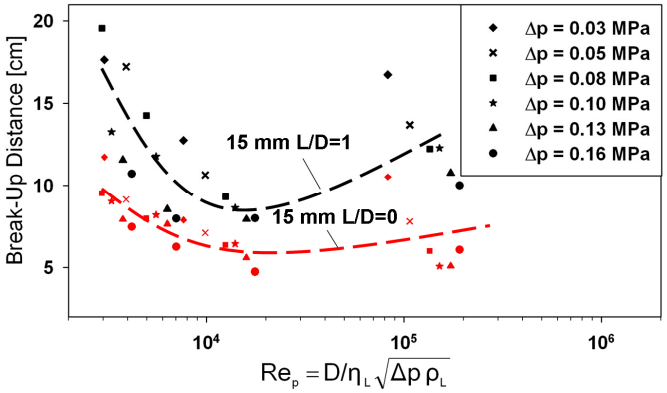

Figure 8: Distance of sheet break-up from nozzle orifice in main flow direction depending on Re_p (15 mm-nozzles)

It is shown that the course of the break-up length within the observed range of Re_p exhibits a global minimum. The minimum is located at Re_p around $1\text{-}2\cdot10^4$. The course is very flat for the short nozzle, i.e. the case of L/D = 0. For a lower

Re_p-number, the break-up length is raising to very high values, as the hydrodynamic friction is increasing. When the Re_p-number is higher than $2 \cdot 10^4$ the course of the break-up length remains nearly unchanged, although there is a slight increase. Considering the influence of the atomization pressure difference, a tendency of shorter break-up lengths can be observed when the pressure is increased. This behaviour is expected, since an increase of the atomization pressure results in higher aerodynamic stimulation of the sheet due to the higher velocities. However, it was unexpected to see a significant difference when the orifice length of the nozzle is changed. Changing the L/D-ratio from 0 to 1, the break-up length of the liquid sheet is rising by around 30-50%. It hardly can be explained by friction forces only. Further investigations on the inner flow conditions have to be made to explain this behaviour.

One challenging investigations on moving sheets is the measurement of the local liquid sheet velocity due to their high speed and short running length before break-up. In the past, measuring of the sheet velocities was tried via PIV [12], but assumed to remain constant along the main flow direction. Newer researches on radial spreading and oscillating sheets however indicate a radial decay of the velocity [13]. However, the operating conditions of the investigated atomizer are almost the same as in the present work. In our case, the current measuring system has a higher time-resolution (11 kHz vs. 250 Hz), and a mutual decrease of the sheet velocity along streamlines, should be detected by the fibre-sensor. The results of the velocity measurements obtained by cross correlation of sensor data are presented in Fig. 9. A sharp edged nozzle orifice with a diameter of 8 mm was deployed. The sheet velocity is plotted for orifice distances between the closest position suitable for data acquisition by the invasive fiber-sensor and the location of sheet break- up. The liquid viscosity was constant at η_L = 1 mPas (pure water). In addition to that, two Bernoulli-velocities are shown as limiting cases of highest possible velocities. Actually, there is a significant decrease in sheet velocity within a distance of 100 mm. At the same time the decay in the sheet velocity is stronger in case of higher differential pressure at the nozzle compared to the conditions at smaller pressure.

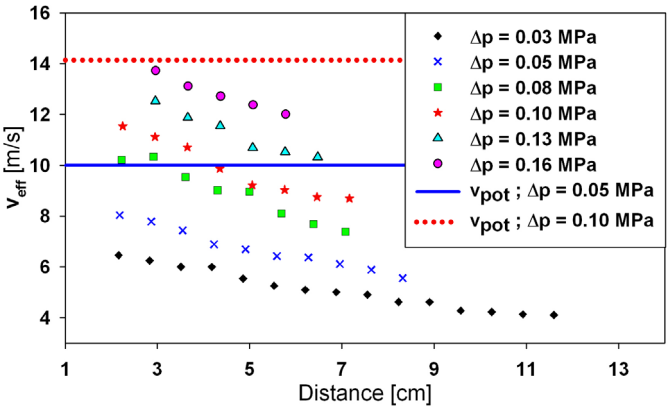

Figure 9: Liquid sheet velocity along the distance from nozzle orifice in flow direction (D=8 mm, L/D = 0, η_L = 1 mPas)

Similar sheet behaviour was also seen using different nozzle geometries, whereas smaller orifice diameters and shorter length to diameter ratios lead to higher exit speeds and also to a stronger decrease in the sheet velocity along its propagation. Comparing the detected velocities to the potential velocity v_{pot} at the corresponding pressure differences, it can be shown, that the relative energy loss due to friction forces inside the nozzle is around 15-25%. When varying the liquid viscosity to higher values at constant atomization pressure (Δp = 0.13 MPa) the detected velocity gradient gets smaller, as shown in Fig. 10. Finally, for higher viscosities, at least for η_L > 10 mPas, the velocity decrease becomes smaller. This may be explained by the smaller exit speed of the liquid at the orifice and the smooth surface and a lower interaction with the environmental gas. But when verifying this assumption to the measured spatial growth (Fig. 7), it turns out that there is still aerodynamic stimulation, since there is distinct growth of disturbances along the sheet, even at higher liquid viscosities.

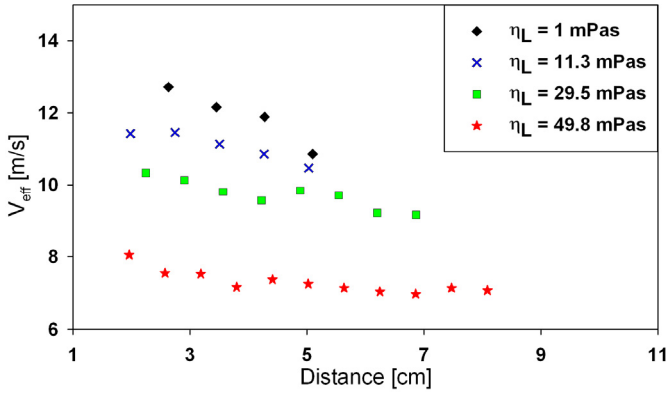

Figure 10: Liquid sheet velocity versus distance from nozzle orifice along the main flow direction (D=15 mm, L/D = 1, Δp = 0.13 MPa)

To understand this behaviour, a closer look on the sheet consistence is necessary. Fig. 11 shows such oscillating sheets, the left one at lower viscosity (pure water), the right one at η_L = 49.8 mPas. Both sheets emerge from the same nozzle geometry. The disturbance level on the low viscous sheet may be caused by superimposed turbulent oscillations. This may be interpreted as a higher surface roughness, as there are some higher frequencies with lower energy content (smaller amplitudes). Meanwhile, the higher-viscid sheet has an almost smooth, clear surface with the appearance of long waves. Evaluating experimental data it is possible to find the correlations predicting the velocity decrease.

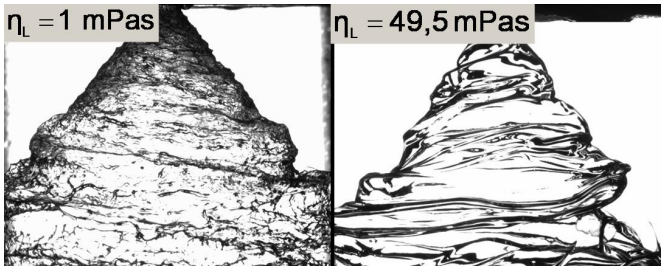

Figure 11: left: sheet roughness of low viscous liquid, right: smooth sheet of high viscous liquid (15 mm, L/D = 1, Δp = 0.10 MPa)

The difference in sheet texture might also be responsible for the sheet behaviour, as the transition from exponential to a linear course of the spatial growth along the streamlines when increasing the liquid viscosity. In order to obtain the velocity at the nozzle orifice, the measured velocities can be

extrapolated towards zero running length. Relating this velocity to the potential velocity v_{pot} results in a dimensionless velocity number φ. Velocity numbers for different nozzle geometries and within a wide range of Re_p are shown in Fig. 12.

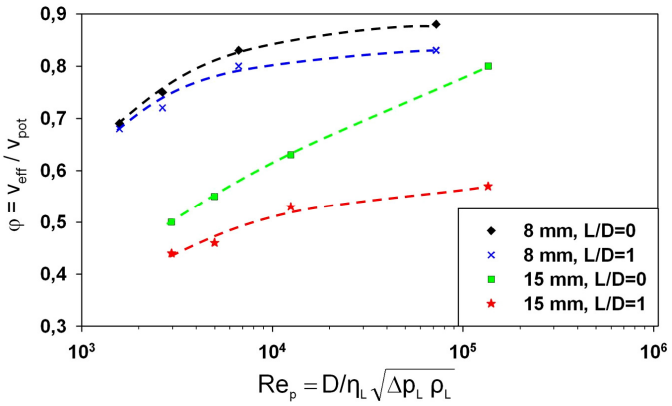

Figure 12: Dimensionless sheet velocity close to the nozzle orifice depending on Re_p

The plot indicates that the velocity number is increasing with an increasing Re_p-number. Nozzles with smaller orifice diameters reach higher velocity numbers, resulting in higher sheet velocities and therefore thinner liquid sheets at the same feed rate. The highest velocity number is around 0.87, which means that at least 13% are dissipated trough turbulence and friction losses. When analyzing the influence of the L/D-ratio, it turns out that nozzles with a sharp edged orifice perform better. This could be attributed to the less disturbed flow at the exit of the nozzle for higher L/D- ratios. With decreasing Re_p-number, the trends of both orifice geometries for particular diameters converge. This indicates that with increasing weighting of friction losses over losses due to turbulence, the geometrical form of the nozzle orifice is becoming negligible.

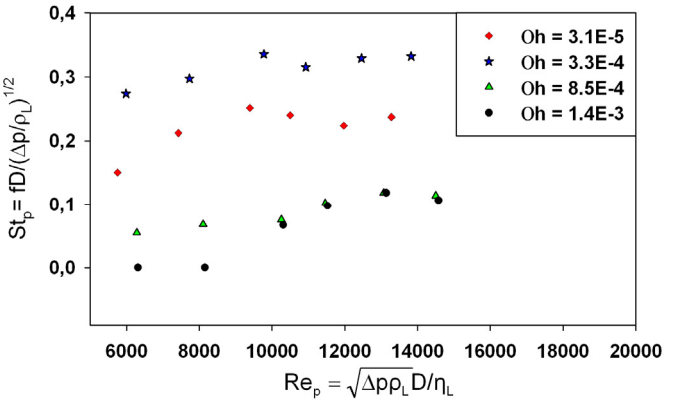

Figure 13: Dimensionless oscillation frequency at break-up location versus Re_p (D=15 mm, L/D = 1)

Fig. 13 presents the results of the frequency analysis for one single nozzle geometry at the location of break-up. These frequencies might be of superior interest, since the droplet diameters are directly linked to them. To transform the oscillation frequency f of the sheet in a dimensionless form, we introduce a pressure based Strouhal in analogy to the pressure Reynolds number Re_p, whereas the velocity is expressed via Bernoulli-equation. The Strouhal number St_p exhibit in the investigated ranges a slightly increase and indicates thus a dependence of the atomization process from Re_p at constant geometrical factors. These Strouhal numbers correspond to a frequency range of 40 up to 300 Hz and lead to wave lengths in the range of 3 > λ > 10 cm. Random oscillations with frequencies up to 500 Hz and higher energy content were found on single locations in the observed time period. However, further investigations have to be made to identify the oscillations responsible for the sheet break-up.

6 CONCLUSIONS

The investigations have shown different characteristics in the growth of aerodynamic waves, depending on the viscosity of the atomized fluid and the geometry of the nozzle. Within the range examined, the Wavelet analysis of the sheet oscillation shows dominating oscillation frequencies at all flow conditions and with all nozzle geometries within the range of 10 < f < 500 Hz. Higher frequencies (> 500 Hz) with higher intensities i.e. amplitudes were not detected. With decreasing viscosities of the liquid, the oscillation frequency rises to higher values. There is also a significant decrease in sheet velocity over its running length, probably caused by an increased "roughness" of the oscillating sheet at lower liquid viscosities and therefore increased interaction with the environmental gas. In this case, the growth rate of the waves can be expressed by an exponential term. At higher viscosities (> 10 mPas), there is only minor velocity decrease of the sheet, because the emerging hollow conical sheet is almost smooth. In this case, the growth of wave amplitude shows an almost linear behavior over the running length of the sheet. With increasing viscosity and decreasing oscillation frequencies, the break-up length of the oscillating increases, until the disintegration mechanism reaches the region of rim contraction.

ACKNOWLEDGMENT

The authors want to express their gratitude to the „Deutsche Forschungsgemeinschaft" for their financial support of the project.

NOMENCLATURE

Symbol	Quantity	SI Unit
a	Snake parameter (stretching)	-
b	Snake parameter (bending)	-
D	Nozzle orifice diameter	m
D_E	Nozzle inlet diameter	m
D_K	Nozzle swirl chamber diameter	m
E_{snake}	Resulting snake energy	-
E_{ext}	External snake energy	-
E_{int}	Internal snake energy	-
E_{user}	User defined snake energy	-
f	Oscillation frequency	1/s
L	Length of nozzle orifice	m
v_{eff}	Sheet velocity	m/s
v_{pot}	Potential sheet velocity	m/s
v(s)	Parametric curve	-
Δp	Pressure difference	Pa
α	Nozzle swirl chamber angle	deg
$η_L$	Dynamic liquid viscosity	kg/(m·s)
$ρ_L$	Liquid density	kg/m³
σ	Surface tension	kg/s²

λ	Oscillation wavelength	m
$\varphi = v_{eff}/v_{pot}$	Velocity-number	-
$Oh = \frac{\eta_L}{\sqrt{D \varrho_L \sigma}}$	Ohnesorge-number	-
$Re_p = \frac{D\sqrt{\Delta p \varrho_L}}{\eta_L}$	Pressure based Reynolds-number	-
$St_p = \frac{f \cdot D}{\sqrt{\Delta p / \varrho_L}}$	Pressure based Strouhal-number	-
$We = \frac{\varrho v^2 D}{\sigma}$	Weber-number	-

REFERENCES

[1] S. B. Squire, Investigation of the Instability of a Moving Liquid Film, *Brit. J. Appl. Phys.*, vol.4, pp. 1967-1969, 1953

[2] N. Dombrowski and W. R. Johns, The Aerodynamic Instability and Disintegration of Viscous Liquid Sheets, *Chem. Eng. Sci.*, vol.18, pp. 203-214, 1963

[3] Senecal at all, Modeling High-Speed Viscous Liquid Sheet Atomizationm, *Int. J. Multipase Flow*, vol. 25, pp. 1073-1097, 1999

[4] C. Mehring and W.A. Sirignano, Capillary Stability Of Modulated Swirling Liquid Sheets, *Atomization and Sprays*, vol. 14, pp. 397-436, 2005

[5] T.J. Tharakan, K. Ramamurthi, Growth of Longitudinal Waves in Plane Liquid Sheets Having Lateral Waves Modes When Exposed to Two Gas Streams of Unequal Velocities, *Atomization and Sprays*, vol. 15, pp. 181-200, 2005

[6] F. Landwehr, H. Wiggers, and P. Walzel, A New Technique for Multi-Phase Spray Analysis at High Loads, *ILASS-Europe 2001*, Zurich, 2-6 Sep., 2001

[7] F. Landwehr, F., Feggeler, D., Walzel, P., Weichert, F., Schröter, S. and Müller, H., A Fibre Sensor Based Frequency Analysis of Surface Waves at Hollow Cone Nozzles, *Experiments in Fluids*, vol. 40, pp. 523-532, 2005

[8] M. Kass, A. Witkin and D. Terzopoulos, Snakes: Active Contour Models, *Int. J. of Computer Vision*, vol. 1, pp. 321-331, 1988

[9] W. Press, S. Teukolsky, W. Vetterling and B. Flannery, Numerical Recipes in C. 2nd edition, *Cambridge University Press*, 1992

[10] M. Gaspar, F. Weichert, H. Müller, E. Musemic, D. Feggeler and P. Walzel , PIV Measurements in Pressure Swirl Atomizers, *IASTED International Conference 2008,* 13-15 Feb., Innsbruck, Austria, 2008

[11] C. J. Clark and N. Dombrowski, Aerodynamic Instability and Disintegration of Inviscid Liquid Sheets, *Proceedings of the Royal Society of London. Series A, Mathematical and Physical Sciences*, vol. 329, No. 1579, pp. 467-478, 1972

[12] P. Broll and P. Walzel, PIV Measurements in Pressure Swirl Atomizers, *ILASS-Europe 2001*, Zurich, 2-6 Sep., 2001

[13] H. Lienemann, J. Shrimpton and E. Fernandes, A Study on the Aerodynamic Instability of Attenuating Liquid Sheets, *Experiments in Fluids*, vol. 42, pp. 241-258, 2007